

Limitations of Fast Charging of High Energy NMC-based Lithium-Ion Batteries: A Numerical Study

Jerzy J. Jasielec^{*[a, b]} and Pekka Peljo^[a]

The aim of this work is to answer the question: how to realize high energy and high-power lithium-ion batteries. Lithium-metal and graphite anodes with nickel manganese cobalt (NMC) cathodes of varying thickness are investigated with finite element modelling. The overpotential analysis is performed to pinpoint the source of losses and the possible ways to decrease them. The electrolyte overpotential, resulting from the salt concentration gradient and leading to saturation and depletion of lithium in parts of the cell is identified as the main factor causing poor specific capacity at high discharge/charge currents. The influence of various parameters, including concen-

tration and transference number of lithium salt in the electrolyte, NMC particle size, electrolyte conductivity and the exchange current density, on the galvanostatic response of modelled battery cells is discussed. The increase of the transference number would improve the performance as this would decrease the electrolyte salt concentration gradient. Lithium depletion effect can be also minimized by elevating the initial electrolyte salt concentration, as well as by increasing the porosity of the cathode, particularly at the cathode/separator boundary.

Introduction

Since the development of first lithium-ion batteries (LIBs) in the 1970s and the first commercial release of LIBs by Sony Corporation in 1991,^[1] we have seen a rapid and continuous development of this type of energy storage devices. By the end of the 20th century LIBs were accounting for 63% of worldwide sales values in portable batteries.^[2] Nowadays these batteries are ubiquitous in everyday life, finding application in a variety of devices from cell phones to electric cars, and therefore providing a profound impact on the development of human society. The significant progress in LIBs can be attributed to the increasing fundamental understanding of the materials and reactions, as well as to technological improvement. Numerous reviews^[1–12] have been written to address and discuss the developments in the field of LIBs as well as various electrode and electrolyte materials.

A battery is composed of one or more interconnected electrochemical cells. Each cell is composed of two electrodes, anode and cathode, separated by the electrolyte solution containing dissociated salts, which enable ion transfer between the two electrodes. The working principle of the electrodes is based on the single-electron reaction, in which Li ions shuttle back and forth between the anode and cathode during the electrochemical redox reaction.^[9] The electrodes can be of the intercalation type or conversion type. The intercalation electrodes are highly reversible and have minimal changes in their crystal structures, while the conversion electrodes break and create chemical bonds during the insertion and extraction of Li ions.^[12] Conversion anodes, such as metallic Li anodes, have specific capacities around 10 times greater than that of a graphite anode.^[12] However, the high reactivity of the Li-metal, which assures the high energetic content, also induces safety hazards and limited cyclability.^[13] For this reason, both the LIBs, which employ Li metal conversion anode and the ones using graphite intercalation anode, receive the intensive interest of the scientific community.

An effective method to enable the development of high energy density LIBs, is to increase the thickness of the electrode, that allows to improve the active to passive material ratio, by lowering the number of layers in the cell stack. The thin NMC cathodes can be referred as the high-power electrodes, i.e., ones capable to operate at high current densities, while the cells with ultra-thick NMC cathodes can be referred as high-energy electrodes, applicable only at lower current densities, due to the transport limitations.^[14] Cells with thick NMC cathodes show significant capacity losses of 37% while cycling at C/2 rate.^[15] The physics-based factors that limit the energy/power density of thick electrodes are the increased cell polarization and underutilization of active materials, caused by Li-ion diffusion in active materials and Li-ion depletion in the electrolyte phase.^[16]

[a] Dr. J. J. Jasielec, Prof. Dr. P. Peljo

Department of Mechanical and Materials Engineering
Faculty of Technology, University of Turku
20014 Turku, Finland
E-mail: jerzy.jasielec@utu.fi
pekka.peljo@utu.fi

[b] Dr. J. J. Jasielec

Department of Physical Chemistry and Modelling
Faculty of Materials Science and Ceramics, AGH University of Science and Technology
Al. Mickiewicza 30, 30-059 Kraków, Poland

 Supporting information for this article is available on the WWW under <https://doi.org/10.1002/batt.202300189>

 An invited contribution to a Special Collection dedicated to NordBatt 2022 conference

 © 2023 The Authors. *Batteries & Supercaps* published by Wiley-VCH GmbH. This is an open access article under the terms of the Creative Commons Attribution License, which permits use, distribution and reproduction in any medium, provided the original work is properly cited.

Several researchers analysed the possible usage of the ultra-thick cells and their limitations. Du et al.^[16] numerically investigated the optimization LiNi_{0.8}Co_{0.15}Al_{0.05}O₂/graphite cell stack and different strategies to overcome the transport limitations of ultra-thick electrodes. Danner et al.^[17] studied thick NMC-graphite LIBs, to computationally assess the effect of inhomogeneities in carbon black distribution and give answers to the possible occurrence of lithium plating during battery charge. Zheng et al.^[18] comparatively investigated the impact of thickness of LiNi_{1/3}Co_{1/3}Mn_{1/3}O₂ and LiFePO₄ electrodes on the rate capability, energy and power density, and attributed the deterioration of long-term cycling performance to the high internal resistance and poor mechanical integrity of thicker electrode. Gallagher et al.^[19] compared the experimental measurements with the theoretical predictions based on concentrated solution and porous electrode theories, showing that the electrolyte transport limits the utilization of the positive electrode at critical C-rates during discharge, and that a combination of electrolyte transport and polarization lead to lithium plating in the graphite electrode during charge. Kremer et al.^[14] analysed the NMC cathode in the half-cell setup and investigated the influence of the lithium concentration in the electrolyte on the specific current capacity of the electrode.

In every battery technology, the measures of its performance (e.g., the cell potential, the capacity or the energy density) are related to the intrinsic properties of the materials that form the anode, the cathode and the electrolyte.^[1] In this paper we numerically investigate the overpotential generated in the cells and the influence of the system parameters on the capacity of the battery cells. The cells in question contain two different types of anodes i.e., conversion (Li-metal) anode and intercalation (graphite) anode and the NMC cathode of different thickness. The analysed parameters of the system include electrolyte salt concentration, electrolyte conductivity, transference number, NMC particle radius, as well as the reaction rates at anode and cathode.

Computational Model

Extending the lifetime of LIBs, increasing their energy density, improving safety, reducing cost, and increasing their charging speed are the issues researched by many scientists all over the world. This creates a necessity for development of tools for theoretical description and numerical simulation of the battery behaviour.

The first models of Lithium-Ion Batteries were developed in 1990s by Newman et al.^[20,21] In these models of the galvanostatic charge/discharge, ionic transport in the 1D battery cross-section has been described using concentrated solution theory, while the electric potential has been calculated using a charge balance based on the Ohm's law. This approach was followed since, with the most significant contribution being the implementation of the model in COMSOL Multiphysics software,^[22] that allowed battery developers and researchers to investigate the theoretical influence of various design parameters without the necessity to develop their own software.

It must be noted that during last decades the vast number of models has been developed and the literature on modelling of LIBs

is very extensive.^[23–26] Some interesting extensions to the original Newman model include e.g., description of thermal effects^[27–29] or the changes in the porosity of the material due to the reversible intercalation processes.^[30,31] Numerous models have been also developed for the purpose of identifying critical material components and their relative impact on the cell performance (i.e., performing the sensitivity analysis). For example, Darling and Newman^[32] utilized the porous electrode theory to account for the effect of parameters like porosity, particle size distribution, thickness of the electrode and properties of the electrolyte on the cell impedance, while Santhanagopalan and White^[33] perturbed the cathode thickness, porosity, tortuosity and the mean particle radius, to reflect the variations during the manufacturing process and their relevance to the cell performance.

In this work, we present a simple 1D Newman-like model for the description of LIBs, which is easy to implement in COMSOL Multiphysics, even for the readers without extensive modelling background. In Supplementary Information we present step-by-step instructions for the implementation of the model described below.

Model Description

Two one-dimensional models with distinct geometries (see Figure 1) have been implemented in COMSOL 6.0 using Battery Design Module.

The classical Newman model^[20,21] has been used. In the separator domain, the electric potential in the liquid phase ϕ_2 , and the lithium ion concentration in the liquid phase c_2 , are given as:

$$\left\{ \begin{array}{l} \nabla \left\{ -\kappa_2 \nabla i_2 + \frac{2\kappa_2 RT}{F} \left(1 + \frac{\partial \ln f_{\pm}}{\partial \ln c} \right) (1 - t_{\pm}) \nabla \ln c_2 \right\} = 0 \\ \frac{\partial c_2}{\partial t} = \nabla (D_{\pm} \cdot \nabla c_2) - \frac{i_2 \cdot \nabla t_{\pm}}{F} \end{array} \right. \quad (1)$$

where κ_2 is the conductivity of the liquid phase, D_{\pm} is the binary diffusion coefficient, f_{\pm} is the mean activity coefficient, t_{\pm} represents the transference number of lithium cation, F is the Faraday constant, R is the gas constant and T denotes temperature and t represents time. The current density in the solution phase, i_2 , is expressed as:

$$i_2 = -\kappa_2^{\text{eff}} \nabla \phi_2 + \frac{2\kappa_2^{\text{eff}} RT}{F} \left(1 + \frac{\partial \ln f_{\pm}}{\partial \ln c} \right) (1 - t_{\pm}) \nabla \ln c, \quad (2)$$

In the porous electrode domains, these variables are affected by the intercalation process. Hence, the electrical potential in the solid

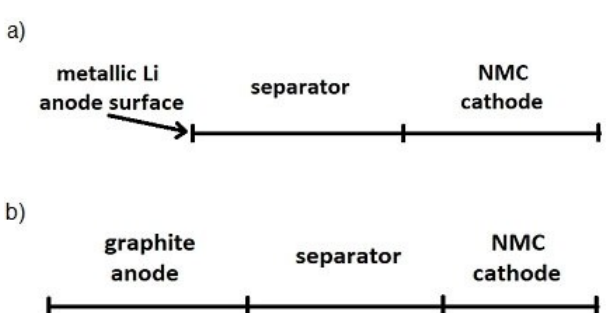


Figure 1. Graphical representation of the model geometries: a) cells with metallic lithium anode, b) cells with porous graphite anode.

phase ϕ_1 , the electric potential in the liquid phase ϕ_2 , and the lithium ion concentration in the liquid phase c_2 are given as:

$$\left\{ \begin{array}{l} \nabla(-\kappa_1^{\text{eff}} \nabla \phi_1) = -S_a i_{\text{loc}} \\ \nabla \left\{ -\kappa_2^{\text{eff}} \nabla \phi_2 + \frac{2\kappa_2^{\text{eff}} RT}{F} \left(1 + \frac{\partial \ln I_{\text{app}}}{\partial \ln c_2} \right) (1 - t_+) \nabla \ln c_2 \right\} = S_a i_{\text{loc}} \\ \varepsilon_2 \frac{\partial c_2}{\partial t} = \nabla(D_2^{\text{eff}} \cdot \nabla c_2) - \frac{i_{\text{loc}} \cdot \nabla t_+}{F} + \frac{1}{F} S_a i_{\text{loc}} (1 - t_+) \end{array} \right. \quad (3)$$

where $S_a = 3\varepsilon_1/r_p$ is the specific interfacial area, i_{loc} represents the local charge transfer current density, $\kappa_1^{\text{eff}} = \kappa_1 \cdot \varepsilon_1^\gamma$ is the effective conductivity of the solid phase, $\kappa_2^{\text{eff}} = \kappa_2 \cdot \varepsilon_2^\gamma$ is the effective conductivity of the liquid phase, and $D_2^{\text{eff}} = D_\pm \cdot \varepsilon_2^\gamma$ is the effective diffusion coefficient, ε_1 is the solid phase volume fraction of electroactive material, ε_2 denotes porosity, and γ is the Bruggeman coefficient, set to $\gamma = 1.5$, which corresponds to packed bed of spherical particles. r_p is the particle radius.

The local charge transfer current density i_{loc} , resulting from the pore wall flux of lithium ions in the porous electrodes (both NMC cathode and graphite anode) is calculated using Butler-Volmer kinetics expression:

$$i_{\text{loc}} = i_0 \cdot (c_{\text{max}} - c_s)^{1-\beta} \cdot c_2^\beta \cdot \varepsilon_s^\beta \left\{ \exp\left(\frac{(1-\beta)F}{RT}\eta\right) - \exp\left(\frac{-\beta F}{RT}\eta\right) \right\} \quad (4)$$

where $\beta = 0.5$ is the symmetry factor, i_0 denotes the reference exchange current density, c_s is the lithium surface concentration and c_{max} is the maximum lithium surface concentration. Note that all these concentrations in the equation above are dimensionless, i.e., c_s and c_{max} are divided by $0.5 \cdot c_{\text{max}}$, while c_2 is divided by 1000 mol/m^3 . The overpotential η is given as:

$$\eta = \phi_1 - \phi_2 - E_{\text{ref}}, \quad (5)$$

where E_{ref} refers to the electrode particle's equilibrium potential, which is a reference potential function dependent on the state of charge (SOC). The open circuit voltage (OCV) is the difference of equilibrium potentials at the positive and the negative side.

The surface concentration of lithium $c_s = c_1(r_p)$, resulting from the intercalation process in porous electrodes is calculated from radial diffusion:

$$\left\{ \begin{array}{l} \frac{\partial c_1}{\partial r} = \nabla(D_1 \nabla c_1) \\ \frac{\partial c_1}{\partial r} = 0 \text{ at } r = 0 \\ -D_1 \frac{\partial c_1}{\partial r} = \frac{i_{\text{loc}}}{F} \text{ at } r = r_p \end{array} \right. \quad (6)$$

where c_1 is the lithium concentration inside the particle, and D_1 is the diffusion coefficient in the solid phase.

In the cells with metallic lithium, the current density i_{loc} , through the anode surface is given as:

$$i_{\text{loc}} = i_0 \cdot c_2^\beta \left\{ \exp\left(\frac{(1-\beta)F}{RT}\eta\right) - \exp\left(\frac{-\beta F}{RT}\eta\right) \right\} \quad (7)$$

where the overpotential is $\eta = \phi_1 - \phi_2$.

There is no liquid phase current flowing through the boundaries of the system, i.e., the electrical insulation boundary condition is applied ($I = 0$). This also implies no ionic transport through the boundaries (the zero-flux condition). At the left boundary of the system, the potential was set to $\phi_1 = 0$, and at the right boundary of the system, the normal current density $I = -I_{\text{app}}$ was set, where I_{app} is the applied current density.

Model parameters

In this paper four types of cells with different type of anode material and different thickness of NMC cathode are investigated. The parameters of these cells, including type of the anode, thickness of NMC cathode and active material (AM) mass loading, are listed in Table 1. The thickness of the electrodes and corresponding active material mass loading follow the values used by Kremer et al.^[14] in order to allow for a comparison of the results.

The porosity of the NMC cathodes was set to $\varepsilon_2 = 0.191$ and the solid phase volume fraction of electroactive material to $\varepsilon_1 = 0.569$. The NMC conductivity is concentration-dependent and given with the function:^[14]

$$\kappa_1 = \exp(-202.91 \times \text{SOC}^4 + 322.38 \times \text{SOC}^3 - 178.24 \times \text{SOC}^2 + 50.07 \times \text{SOC} - 13.47) \quad (8)$$

where SOC represents the state of charge.

The diffusion coefficient of lithium in the NMC phase was set to $D_1 = 2 \times 10^{-13} \text{ m}^2/\text{s}$ and the NMC particle size was set to $r_p = 10 \mu\text{m}$. In all cathodes, the reference potential function for NMC 622, $\text{LiNi}_{0.6}\text{Mn}_{0.2}\text{Co}_{0.2}\text{O}_2$ (COMSOL database) shown in Figure S1(a) was used. The minimum operational SOC was 0.258 and the maximum operational SOC was 0.917, which corresponds to lithium concentrations of 12.3 M and 43.7 M, respectively. The initial concentration of lithium in the solid phase was set to 15 M for discharge and 40 M for charge simulations, which corresponds to SOC=0.315 and 0.839, respectively.

The thickness of the graphite anodes was set to $L_{\text{neg}} = 180 \mu\text{m}$. The porosity of graphite was calculated as $\varepsilon_2 = 0.271$ and the solid phase volume fraction of electroactive material as $\varepsilon_1 = 0.614$. The Li diffusion coefficient, conductivity function and the reference potential function for Graphite, Li_{x}C_6 MCMB (COMSOL database) shown in Figure S1(b) were used. The graphite particle size was set to $r_p = 10 \mu\text{m}$. The minimum operational SOC was 0 and the maximum operational SOC was 0.98, which corresponds to lithium concentrations of 0 M and 30.9 M, respectively. The initial concentration of lithium in the solid phase was set to 30 M for discharge and 10 M for charge simulations, which corresponds to SOC=0.952 and 0.317, respectively.

Table 1. Parameters of the cells used in the numerical simulations.

Cell number	Anode material	Thickness of NMC cathode [nm]	AM mass loading [mg/cm ²]	1 C rate [mAh/cm ²]
Cell 1	metallic Li	22	5.2	0.914
Cell 2	Graphite	22	5.2	0.914
Cell 3	metallic Li	161	46	8.087
Cell 4	Graphite	161	46	8.087

For the graphite and MNC electrodes, the reference exchange current density was set to $i_0 = 1 \text{ A/m}^2$, while for the metallic lithium anode it was set to $i_0 = 0.01 \text{ A/m}^2$.

The thickness of the separator was $L_{\text{sep}} = 100 \mu\text{m}$. The concentration-dependent parameters of the electrolyte, including the conductivity liquid phase κ_2 , the binary diffusion coefficient $D_{\pm,1}$, the transference number t_+ and the thermodynamic factor $(1 + \frac{\partial \ln f_\pm}{\partial \ln c})$ are described using the correlations obtained by Kremer et al. (Figure S3 in Ref. [14]). The initial concentration of the electrolyte salt was $c_{2,0} = 1 \text{ M}$.

The temperature of the system was set to 293.15 K and the applied current density was varied in the range $I_{\text{app}} = \pm 1 \text{ mA/cm}^2$ to $I_{\text{app}} = \pm 20 \text{ mA/cm}^2$ (negative for discharge and positive for charge).

Model drawbacks

The used model is supported on parameters values from the literature or empirically assumed. Despite its simplicity, this model describes the mass transfer with high accuracy.

However, some concerns about the model and consequently the extent one can trust the recommendations arising from it to optimize the electrochemical performance maybe raised, i.e.: the description of the reactions kinetics is not fully satisfactory, as the quantitative data on exact reaction mechanisms are scarce; more parameters can depend on the state of charge of the active materials, and for some of them the data is not measured; the description of the electrical conductivity is not fully satisfactory for a mixture of poorly conductive active material mixed with conductive additives.

Furthermore, the effects such as high stress due to volume expansion, solid electrolyte interface (SEI) layer formation, lithium diffusion through the SEI layer, gas evolution, etc., have not been considered.

Another issue is that the active material is formulated as small primary particles forming bigger secondary particles, while in the model this is described with an effective particle size, so some discrepancies could occur especially at high currents. The effects of the particle-size distribution can be examined e.g., using the model presented by Meyers et al.^[34]

Results and Discussion

The galvanostatic discharge and charge curves for all cells and applied currents in the range ± 1 to $\pm 20 \text{ mA/cm}^2$, have been calculated (see Figure S2). This corresponds to a charge/discharge rate of roughly 1 C to 20 C for the cells with thin cathode and C/8 to 2.5 C for the cells with ultra-thick cathode. Based on the obtained galvanostatic curves, the relative discharge and charge capacity has been calculated and presented in Figure 2. In all four types of the analysed batteries the high values of the charge current lead to worsening of the total charge capacity. This effect is significantly stronger for the cells with ultra-thick NMC cathodes. While the cells with thin cathodes retain around 90% of the low-current capacity even at the very high currents, the capacity of cells with ultra-thick cathodes decreases significantly with the increasing applied current, for currents higher than 7 mA/cm^2 . Cells with the

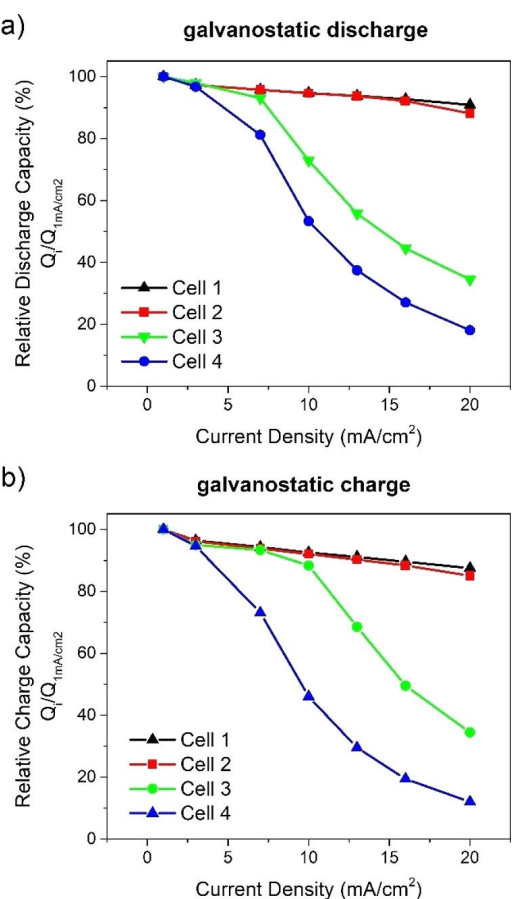


Figure 2. The relative a) discharge capacity and b) charge capacity if the investigated battery cells.

conversion anode, i.e., metallic lithium show better capacity retention than the cells with graphite intercalation anode.

This improvement is significant for the cells with ultra-thick cathode (12–19% of initial capacity, at currents higher than 7 mA/cm^2) and very minor for the cells with the thin cathodes (less than 3% of initial capacity for 20 mA/cm^2 currents).

Observing the galvanostatic curves (Figure S2), one can notice that increasing the current density leads to the decrease of the cell potential during the galvanostatic discharge and increase of the cell potential for galvanostatic charge. This effect corresponds to the increase of the overpotential of the cell (negative for discharge and positive for charge).

Overpotential analysis

The total overpotential η_{tot} is the difference between the battery output voltage $E(t)$ under non-equilibrium conditions and the equilibrium potential E_{ref} [see Eq. (5)]. η_{tot} is composed of the following components:^[35]

1. The concentration overpotential at the cathode composed of two terms:

1.1. the potential difference between the particle surface equilibrium potential and the average particle equilibrium potential

$$\eta_d = E_{\text{ref},\text{pos}}(1 - C_s)|_{x=L_{\text{sum}}} - E_{\text{ref},\text{pos}}(1 - C_{\text{av}})|_{x=L_{\text{sum}}}$$

1.2. overpotential caused by non-uniform average lithium concentrations in the electrode

$$\eta_r = E_{\text{ref},\text{pos}}(1 - C_{\text{av}})|_{x=L_{\text{sum}}} - E_{\text{ref},\text{pos}}(\overline{C_{\text{av}}}),$$

where $\overline{C_{\text{av}}} = \frac{1}{L_{\text{pos}}} \int_{L_{\text{neg}}+L_{\text{sep}}}^{L_{\text{sum}}} C_{\text{av}}(x) dx$

2. The concentration overpotential at the anode composed of two terms:

2.1. the potential difference between the particle surface equilibrium potential and the average particle equilibrium potential

$$\eta_{d,\text{neg}} = E_{\text{ref},\text{neg}}(C_s)|_{x=0} - E_{\text{ref},\text{neg}}(C_{\text{av}})|_{x=0}$$

2.2. overpotential caused by non-uniform average lithium concentrations in the electrode

$$\eta_{r,\text{neg}} = E_{\text{ref},\text{neg}}(C_{\text{av}})|_{x=0} - E_{\text{ref},\text{neg}}(\overline{C_{\text{av}}}),$$

where $\overline{C_{\text{av}}} = \frac{1}{L_{\text{neg}}} \int_0^{L_{\text{neg}}} C_{\text{av}}(x) dx$

3. The electrolyte overpotential $\eta_{el} = \phi_2(L_{\text{sum}}, t) - \phi_2(0, t)$ composed of three terms corresponding to cathode, separator and anode, respectively:

$$3.1. \eta_{el,\text{pos}} = \phi_2(L_{\text{sum}}, t) - \phi_2(L_{\text{sep}} + L_{\text{neg}}, t)$$

$$3.2. \eta_{el,\text{sep}} = \phi_2(L_{\text{sep}} + L_{\text{neg}}, t) - \phi_2(L_{\text{neg}}, t)$$

$$3.3. \eta_{el,\text{neg}} = \phi_2(L_{\text{neg}}, t) - \phi_2(0, t)$$

(only for cells with graphite anode)

4. The kinetic overpotential related to the charge-transfer reactions at the interfaces

$$\eta_k = \phi_1 - \phi_2 - E_{\text{ref}}(1 - C_s)$$

5. The pure electrode ohmic contribution (contact impedance overpotential) $\eta_Q = I_{\text{app}} \cdot R_c$. In the presented model this term is neglected, i.e., $\eta_Q = 0$.

During slow discharge ($I_{\text{app}} = -1 \text{ mA/cm}^2$) and slow charge ($I_{\text{app}} = 1 \text{ mA/cm}^2$), the overpotential of all four cells behave in the same way (see Figure 3 and Figure S2, respectively). During the discharge, the main contributor to the total overpotential η_{tot} is the kinetic overpotential η_k . During majority of the process duration, it is constant and low. However, at the end of discharge, the kinetic potential and consequently the total overpotential increases until the cut-off potential of the cell is reached.

During fast discharge ($I_{\text{app}} = -20 \text{ mA/cm}^2$) and fast charge ($I_{\text{app}} = 20 \text{ mA/cm}^2$), the cells with thin NMC cathode show different behaviour than ultra-thick cathode (see Figure 3 and Figure S2). In the cells with thin cathode, several terms contribute to the total overpotential, including the kinetic overpotential η_k , the concentration overpotential resulting from diffusion in the particles of the cathode η_d , the electrolyte potential in the separator $\eta_{el,\text{sep}}$, and (for the cells with graphite electrode) electrolyte potential in the anode $\eta_{el,\text{neg}}$. In the cells with ultra-thick cathode, the major contributor to the total overpotential is the electrolyte potential in the separator $\eta_{el,\text{sep}}$, that reaches high negative values (c.a. -1 V) already at the beginning of discharge and eventually causes the cell potential to reach its cut-off value at three and six times lower total current densities, for cell with metallic Li anode and cell with the graphite anode respectively. In the cell with graphite electrode, electrolyte potential in the anode $\eta_{el,\text{neg}}$ also contributes to the total overpotential.

The analysis above suggests that the behaviour of the electrolyte is the main contributor to the overpotential responsible for the worsening of the total capacity of the cells with ultra-thick cathode.

Therefore, the influence of several parameters of the electrolyte, including lithium concentration, conductivity and transference number, will be discussed in the following sections.

Electrolyte salt concentration

The increase in the applied current leads to the increase of lithium concentration gradient in the electrolyte (see Figure 4). During discharge, this gradient leads to low concentration in the electrolyte in the pores of the NMC cathode. The gradient is significantly bigger in the cells with the ultra-thick cathode, leading to the depletion of lithium (i.e., concentration values close to 0) in the pores of the cathode. The depletion of lithium can be considered the main cause of the electrolyte overpotential, and as a consequence the total capacity reduction in the cells with ultra-thick cathodes.

While during the discharge, the concentration in the pores of NMC cathode is low, during the charge process it reaches very high values. In the cells with ultra-thick NMC cathode, the electrolyte concentration in the vicinity of cathode/current collector boundary exceed the value of 3.4 M , which can lead to the precipitation of LiPF_6 salt. The precipitation would occur for cell 2 and cell 4, when the applied charge current is 7 mA/cm^2 or higher.

In most applications, the electrolyte salt concentration in battery cells is around 1 M , where the ionic conductivity reaches the maximum value and the trade-off between a large number of dissociated ions and a moderate viscosity is attained.^[14,36] Despite the lower conductivity, the electrolytes with salt concentration higher than 1 M have been recently researched by several groups. It has been demonstrated that the increase of electrolyte concentration allows to mitigate the lithium depletion effect occurring in thick electrodes operated at high

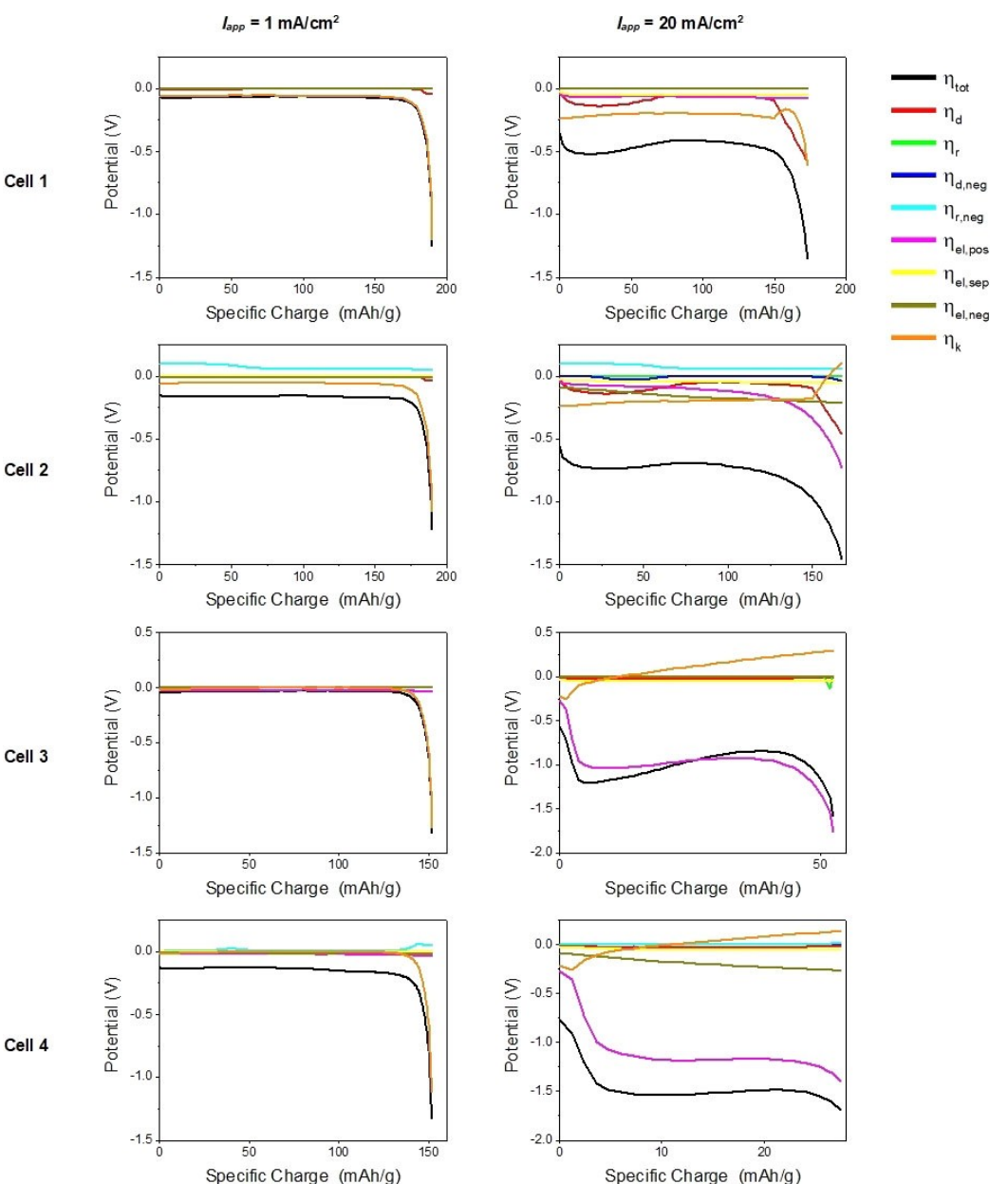


Figure 3. The total overpotential and contribution of overpotential terms, during galvanostatic discharge of four investigated cells with applied current densities in the range 1 to 20 mA/cm².

current densities.^[14,16,37] Highly concentrated electrolytes also show several other properties that can improve the overall response of the electrochemical cell, including an increased oxidative and reductive stability, fast and reversible Li-ion insertion/extraction, the suppression of dendrite formation and inhibition of Al current collector corrosion.^[38–40]

The influence of the electrolyte salt concentration has been investigated and it is shown in Figure 5. The specific discharge capacity of the cells with thin NMC cathode show no dependence on the electrolyte salt concentration (unless it is lower than 1 M, which worsens the capacity if the intercalation graphite anode is used). These results agree with the measurements of Kremer et al.^[14] for the cell composed of lithium foil anode and thin (22 µm) NMC 622 electrode.

For the cells with ultra-thick NMC cathode, one can observe an improvement in capacity at high current densities, when the concentration is elevated. In cell 3 (lithium metal anode + ultra-thick cathode), the capacity increases with the increase of the salt concentration, reaching the best response for the highest value of concentration (i.e., 2.3 M). In cell 4 (graphite anode + ultra-thick cathode), the highest capacity is obtained for the salt concentration of 1.4 M and begins to decrease with the further increase of salt concentration.

These results are in qualitative agreement with the measurements of Kremer et al.,^[14] who have investigated a cell with lithium foil anode and ultra-thick NMC 622 cathode. However, they have obtained the highest specific discharge capacity for the electrolyte salt concentration equal to 1.9 M.

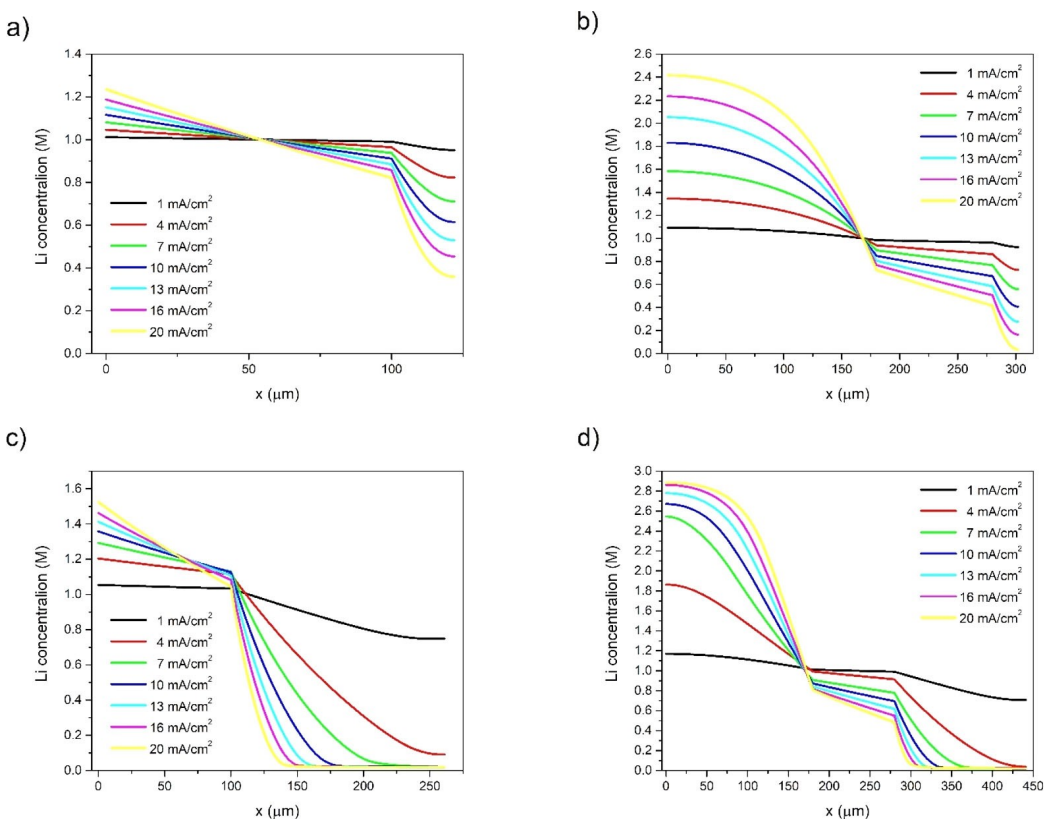


Figure 4. The electrolyte salt concentration during galvanostatic discharge (last time-step) of four investigated cells a) cell 1, b) cell 2, c) cell 3, and d) cell 4; with applied current densities in the range 1 to 20 mA/cm².

Because most of the parameters used in this work follow the ones used by Kremer et al., the difference in the value of the optimal concentration might result from the following reasons:

1. The initial concentrations used in the calculations are different.
2. The reference potential functions for NMC 622 and graphite used here (taken from COMSOL database) differ from the ones used by Kremer et al.
3. The intercalation equation used by Kremer et al. follows the work of Latz and Zausch^[41] and does not include the information about unoccupied lithium sites in NMC structure, i.e., the factor $(c_{\max} - c_s)^{1-\beta}$ is omitted [see Eq. (4)].
4. The kinetic parameters (reference exchange current density) used in the calculations were different, although as will be shown later this should not affect the results.
5. This work uses a simplified 1D model, while Kremer et al. uses 3D model with realistic virtual microstructures which are developed based on tomography data.

The cells' response during charge is slightly different than the one during discharge (see Figure S4). The cells with thin NMC cathodes show the highest specific charge capacity when the electrolyte salt concentration is kept in the range from 1 M to 1.4 M. Further increase of the electrolyte salt concentration worsens the capacity, when the current density is higher than c.a. 10 mA/cm. The cells with ultra-thick NMC cathode show similar response during charge to the discharge response of

cell 4, i.e., the highest capacity is obtained for the salt concentration of 1.4 M and begins to decrease with the further increase of salt concentration. It is also worth mentioning that when the electrolyte salt concentration is increased to 1.4 M or more, the precipitation of the LiPF₆ salt can occur (for both cell 3 and cell 4) at the applied currents of 4 mA/cm² and higher.

Electrolyte conductivity

In order to test the influence of the electrolyte conductivity on the charge capacity of the cell, the concentration-dependent conductivity changed in the range $0.01 \cdot \kappa(c)$ to $100 \cdot \kappa(c)$, where $\kappa(c)$ is the correlation obtained by Kremer et al. (Figure S3 in Ref. [14]). Experimentally the electrolyte conductivity could be modified e.g., by utilisation of different solvents, or by the addition of a salt containing a cation different than lithium, which leads to the ionic-strength of the electrolyte solution, and consequently the conductivity to be less dependent on the concentration of lithium.

The specific discharge and charge capacity of the analysed cells is shown in Figure 6 and Figure S5, respectively. Increase of the conductivity above the value of $\kappa(c)$ has no influence on the discharge and charge capacity of the cells with thin NMC cathode and leads to the minor increase of the discharge and charge capacity (by few %) of the cells with ultra-thick cathodes.

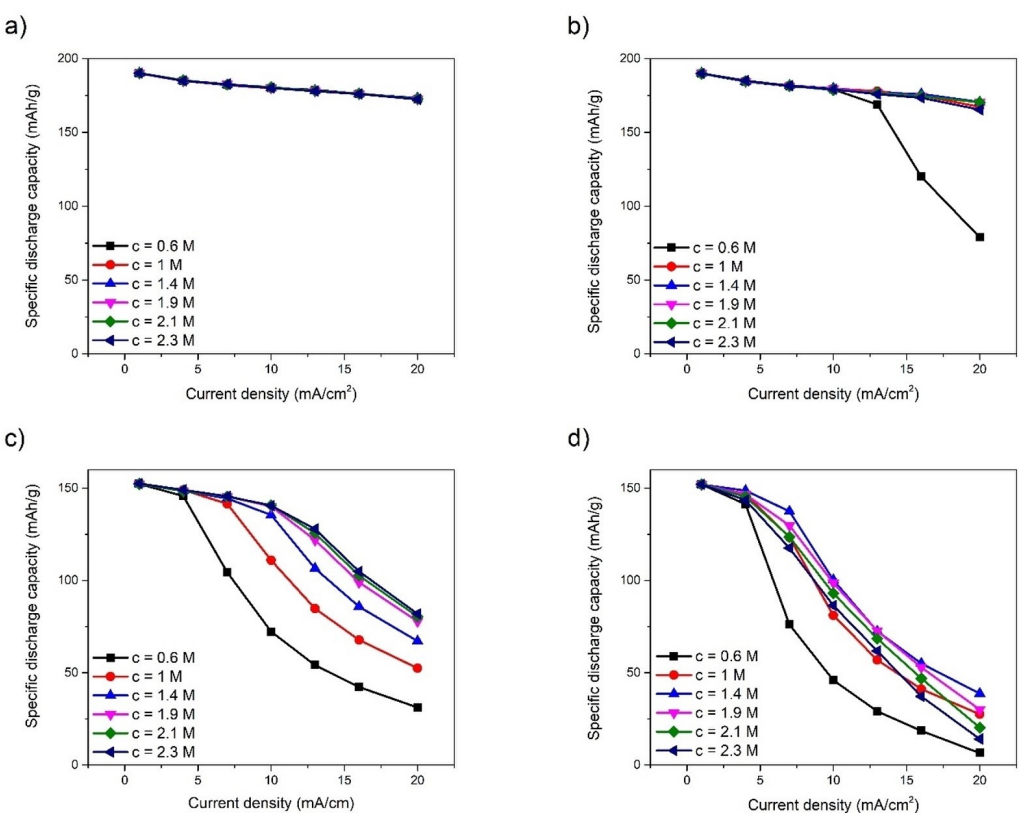


Figure 5. Specific discharge capacity of the battery cells a) cell 1, b) cell 2, c) cell 3, and d) cell 4; as a function of the applied current. Calculations performed for the electrolyte salt concentration changed in the range 0.6 M to 2.3 M.

However, lowering the conductivity below the value of $\kappa(c)$ (or below $\kappa(c)/10$ in the case of cell 1) results in the significant decrease of the charge capacity for all investigated types of cells.

It should be noted that the increase of the conductivity (e.g., to $100 \cdot \kappa(c)$), can lead to numerical instabilities of the models, resulting in "reaching singularity."

The $\kappa(c)$ function reaches its maximum value of 0.95 S/m (for salt concentration of 0.9–0.95 M – see Figure S3 in Ref. [14]). As shown in a recent review,^[42] the typical conductivity of liquid electrolytes is in the range 0.1–1 S/m, while the conductivity of solid electrolytes used in LIBs can vary in the range 10^{-6} –0.1 S/m.

The conductivity can be improved e.g., by increasing the molecular diversity in electrolytes, which essentially leads to high-entropy electrolytes. As very recently reported by Kim et al.,^[43] in weakly solvating electrolytes, the entropy effect reduces ion clustering, that leads to a twofold improvement in ionic conductivity compared with conventional weakly solvating electrolytes.

Transference number

In order to investigate the influence of the transference number on the discharge and charge capacity, the transference number has been set to $t_+ = 1$ (instead of the concentration-dependent

function given by Kremer et al.^[14]). In the engineering practice achieving the transference number equal to one could be achieved by using the separator with immobile anionic sites, instead of the conventional electrolyte, although this would most likely limit the conductivity.

Based on the obtained galvanostatic curves, the relative discharge and charge capacity has been calculated and shown in Figure 7. One can very easily notice that although the effect of worsening of the total capacity at high currents remains present, it is much weaker than in the case of concentration-dependent t_+ .

All cells retain around 90% of the low-current capacity even at the very high discharge currents. During charging, the 85% of initial capacity is retained for all the cells, except cell 4 (which retains around 65% of low-current capacity). This is a significant improvement of capacity retention for the cells with ultra-thick cathodes. Cell 3 (ultra-thick cathode and conversion anode) achieves the capacity retention comparable to the cells using high-power (thin) cathodes, i.e., cell 1 and cell 2.

The improved high-current capacity for systems with the transference number equal to 1, can be attributed to the absence of concentration gradient in the electrolyte. In all of the considered cases the calculated Li-ion concentration in the electrolyte is constant in space and time during entire discharge/charge process (namely $c = 1$ M). The absence of the concentration gradient leads to the significantly lower electrolyte overpotential, but also eliminates the effect of lithium

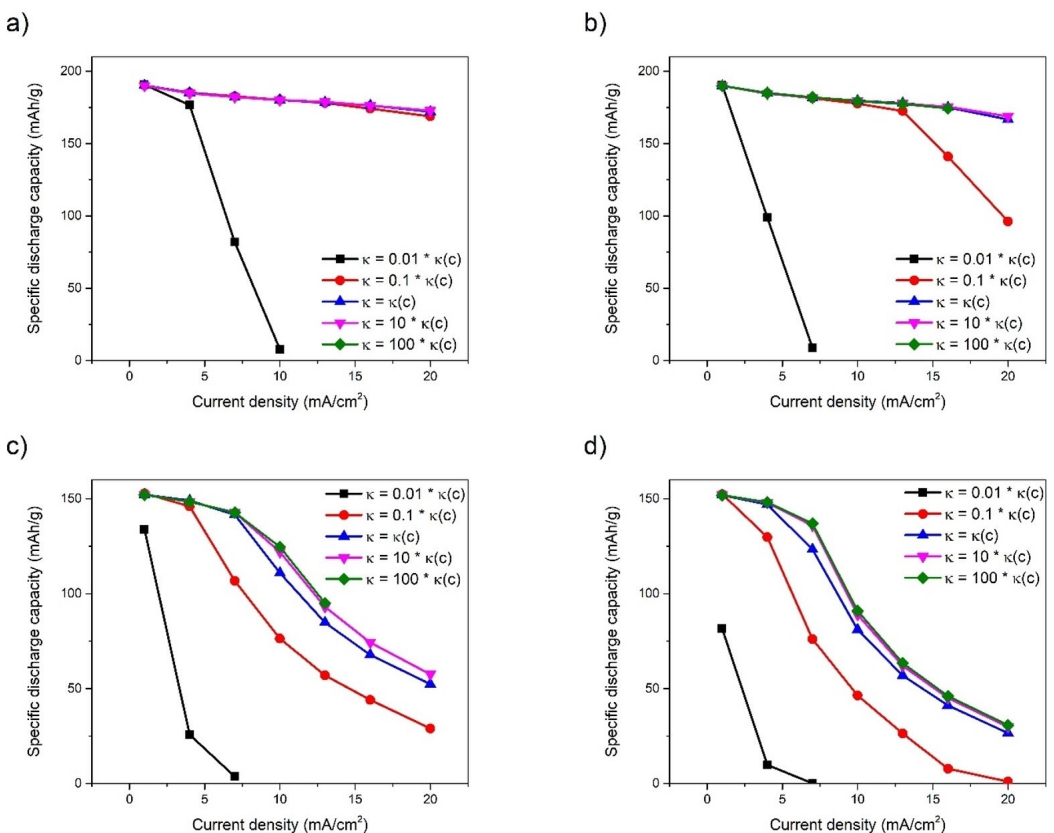


Figure 6. Specific discharge capacity of the battery cells a) cell 1, b) cell 2, c) cell 3, and d) cell 4; as a function of the applied current. Calculations performed for the conductivity of the electrolyte changed in the range $0.01 \cdot \kappa(c)$ to $100 \cdot \kappa(c)$, where $\kappa(c)$ is the correlation obtained by Kremer et al. (Figure S3 in Ref. [14]).

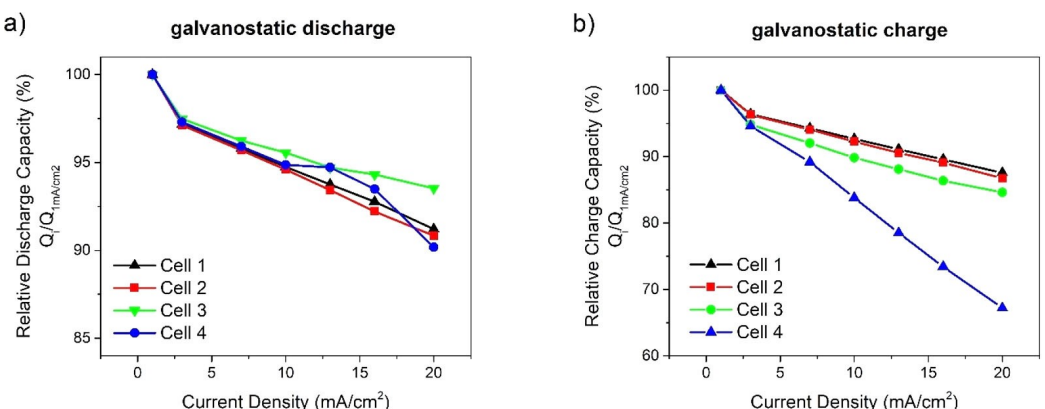


Figure 7. The relative a) discharge capacity and b) charge capacity of the investigated battery cells.

depletion, i.e., the main effect responsible for the poor capacity retention of the cells with ultra-thick NMC cathodes.

Particle radius

One of the parameters, which is relatively easy to modify in the experimental setup is the NMC particle radius. In this study the particle radius inside the cathode was changed in the range of

0.1 μm to 100 μm. The resulting discharge and charge capacities are shown in Figure 8 and Figure S6, respectively. The charge and discharge responses of all four analysed cells are very similar. The change of the radius between 0.1 μm and 1 μm has no effect on discharge/charge capacity of the cells. When the particle radius is increased to 10 μm, a small decrease of the specific capacity (less than 2%) is observed at high discharge/charge currents. Further increase of the particle

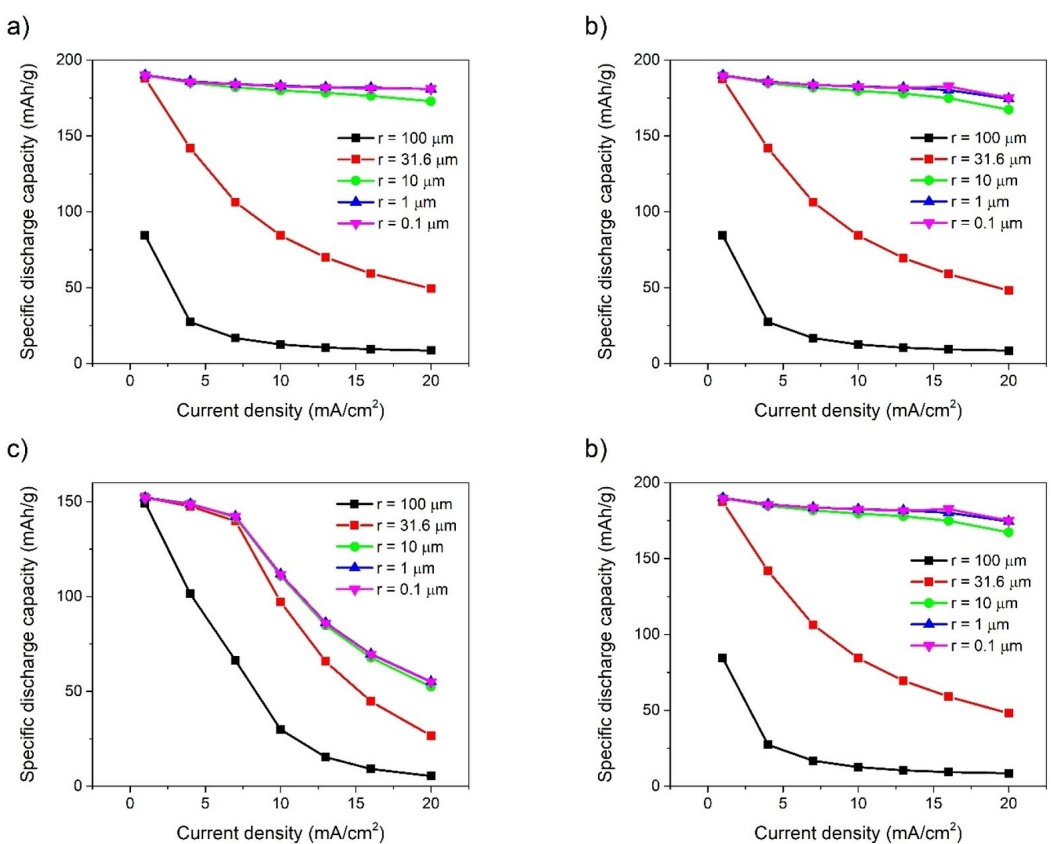


Figure 8. Specific discharge capacity of the battery cells a) cell 1, b) cell 2, c) cell 3, and d) cell 4; as a function of the applied current. Calculations performed for the NMC particle radius in the range 0.1 μm to 100 μm.

radius to 100 μm leads to very significantly lower specific capacity of all the cells, even at relatively low currents.

Hence, the particle radius in the NMC cathode should be kept below a threshold value, lower than 10 μm in order to achieve the optimal response of the cell. This agrees with the observations of Wood et al.,^[44] who noticed that changing the cathode active material particle size from 12 μm to 6 μm improved the 2 C discharge capacity by the factor of 1.8.

It should be noted that similar effect to the increase of the particle radius (r_p) can be achieved by decrease of the solid-state diffusion coefficient (D_s) inside the particle. The response changes resulting from lowering r_p by one order of magnitude can be also achieved by increasing D_s by two orders of magnitude.

Hence, the response of the system depends on the value of parameter $\Delta = \frac{D_s}{r_p^2}$, and not on the individual values of D_s and r_p . However, in the real-life systems, the particle size is significantly easier to modify during the electrode preparation than the diffusion coefficient.

Typical radius of MNC active material particle is 5–20 μm^[45] and the commercial NMC powder contain the particles with the size varying between 6.6–24.11 μm.^[46] However, the preparation and detailed characterization of NMC active materials with primary particle sizes as small as 0.3–1.2 μm have been presented recently by Wagner et al.^[47]

The reference exchange current density (reaction rate)

In order to investigate the influence of the reaction rate on the capacity of the cell, the simulations with the reference exchange current density (reaction rate constant) at the positive electrode in the range 0.1 A/m² to 100 A/m² has been performed. The results during discharge and charge of the cells are presented in Figures S7 and S8, respectively. The change of the reaction rate constant has no influence on the discharge and charge capacity of all four cells.

The influence of the reference exchange current density (reaction rate constant) at the negative electrode has been investigated as well. The results of the simulations, presented in Figures S9 and S10, clearly show that the anodic reaction rate constant has no influence on the specific charge and discharge capacity of the analysed cells.

Solid phase conductivity

In order to test the influence of the solid phase conductivity on the charge capacity of the cell, the SOC-dependent conductivity changed in the range $0.01 \cdot \kappa(\text{SOC})$ to $100 \cdot \kappa(\text{SOC})$, where $\kappa(\text{SOC})$ is the correlation obtained by Kremer et al.^[14] [see Eq. (8)].

The specific discharge and charge capacity of the analysed cells is shown in Figure 9 and Figure S11, respectively. Increase of the conductivity above the value of $\kappa(\text{SOC})$ has small influence on the discharge and charge capacity of all the investigated cells and leads to the minor increase of the discharge and charge capacity (by few %). However, lowering the conductivity below the value of $\kappa(\text{SOC})$ (or below $\kappa(\text{SOC})/10$ when discharging cells 1 and 2) results in the significant decrease of the charge capacity for all investigated types of cells.

The $\kappa(\text{SOC})$ function reaches its maximum value of 0.02 S/m (for SOC=0.68). The NMC materials, in general, have poor electronic conductivity ranging from 10^{-5} to 1 S/m at different states of charge.^[48] The electronic conductivity can be improved by using the conductive additives. However, the content of such additives needs to be minimized for optimum volumetric energy density.

Carbon black (CB) is the most commonly used conductive additive. However, large quantities of CB are necessary to achieve the required electronic conductivity.^[49,50] Substitution of CB with carbon nanotubes (CNTs) results in one order of magnitude improvement in electrode conductivity.^[51] Hence, the use of various types of CNTs as a conductive additive has been investigated by several research groups.^[52–55]

Porosity

Another parameter, which is relatively easy to modify in the experimental setup is the porosity of the electrodes. In this study the porosity inside the cathode was changed in the range 9.1% to 29.1%. The resulting discharge and charge capacities are shown in Figure 10 and Figure S12, respectively.

For the cells with thin cathodes, the porosity does not affect the charge and discharge capacity as long as it is kept above certain threshold ($\varepsilon_2 = 14.1\%$ for cell 1 and $\varepsilon_2 = 19.1\%$ for cell 2). Lowering the porosity below that threshold leads to the decrease of the capacity when the applied current is high (fast charge/discharge).

For the cells with ultra-thick cathodes, the increase of the porosity leads to the increase in the specific charge/discharge capacity of cell 3 and discharge capacity of cell 4, facilitating the fast charging.

Interestingly the relation between the porosity and the charge capacity of cell 4 is more similar to the response shown by cells with the thin cathodes, with clearly visible threshold at $\varepsilon_2 = 19.1\%$.

Note, that in the presented calculations, the solid phase volume fraction of electroactive material was independent of the porosity and kept at the constant value of $\varepsilon_1 = 61.4\%$. In the experimental setup, however, the increase of the porosity is connected to the decrease of the solid phase volume fraction of

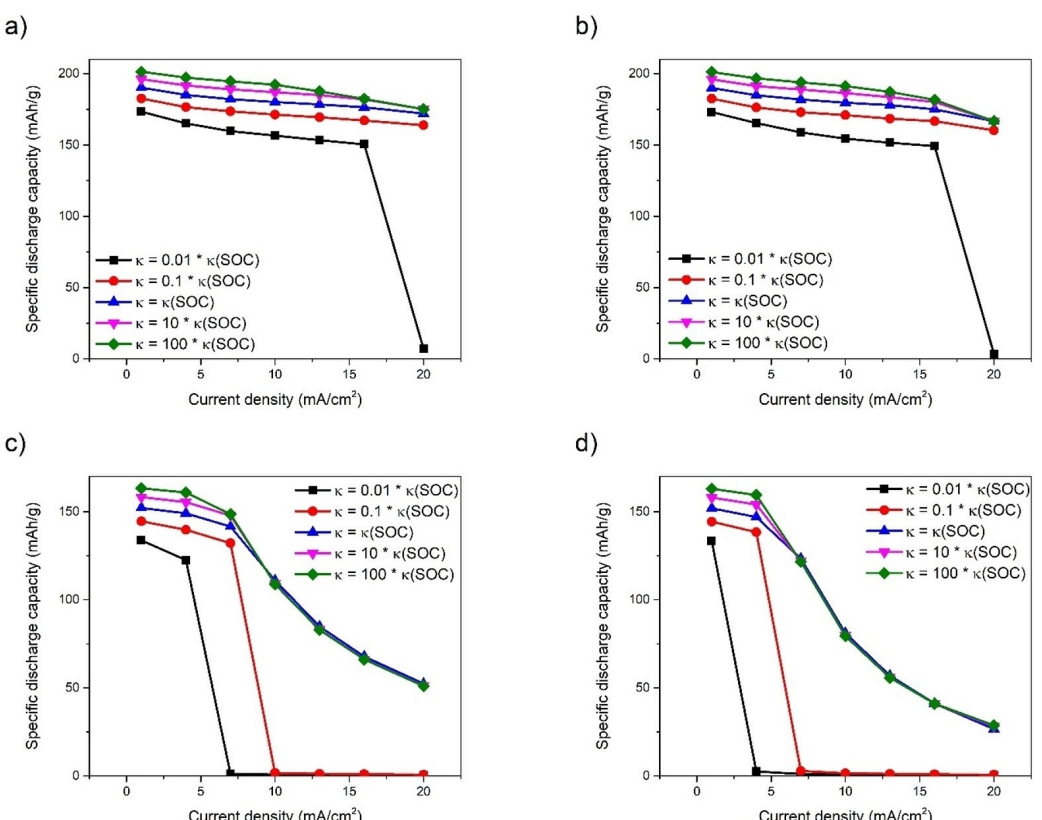


Figure 9. Specific discharge capacity of the battery cells a) cell 1, b) cell 2, c) cell 3, and d) cell 4; as a function of the applied current. Calculations performed for the conductivity of the NMC electrode changed in the range $0.01 \cdot \kappa(\text{SOC})$ to $100 \cdot \kappa(\text{SOC})$, where $\kappa(\text{SOC})$ is given by Eq. (8).

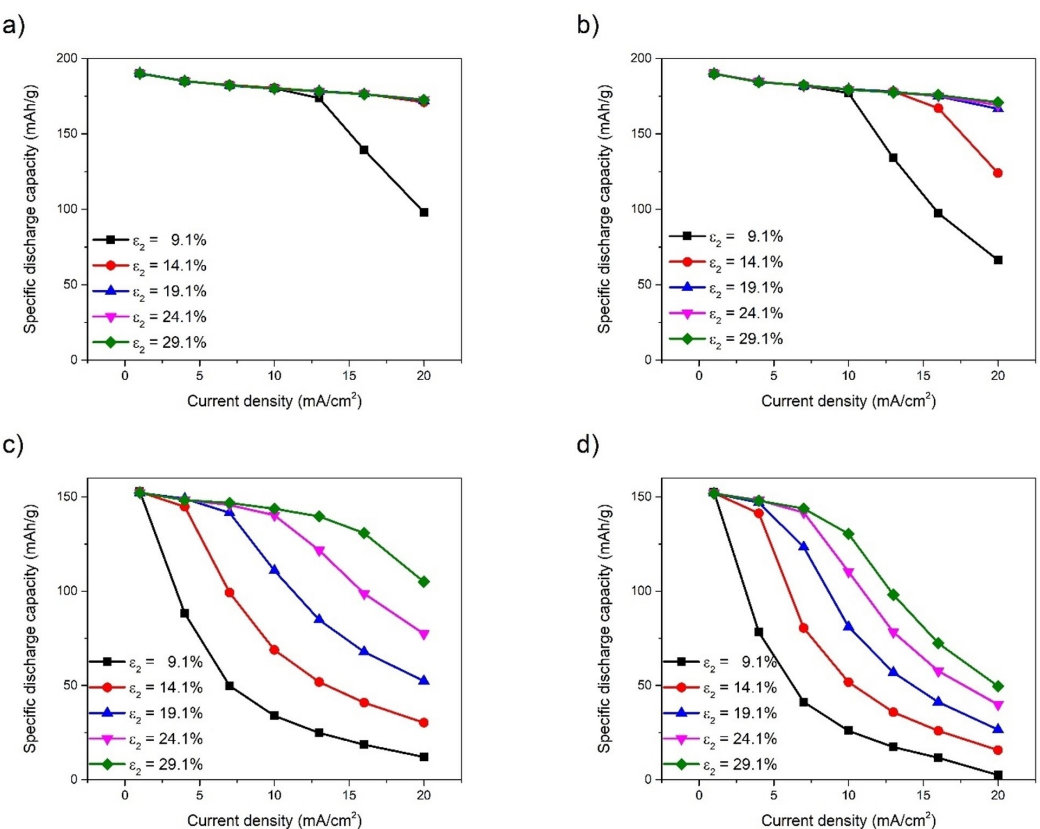


Figure 10. Specific discharge capacity of the battery cells a) cell 1, b) cell 2, c) cell 3, and d) cell 4; as a function of the applied current. Calculations performed for the porosity of the NMC electrode changed in the range 9.1% to 29.1%.

electroactive material. Less electroactive material means lower capacity.

In order to increase the porosity while keeping the total amount of electroactive material constant, the thickness of the electrode would need to be increased.

Tortuosity and Bruggeman coefficient

The common practice to define the tortuosity factor, τ , for the porous media is:

$$\frac{D_{\text{eff}}}{D} = \frac{\tau}{\varepsilon} \quad (9)$$

where D is the diffusion coefficient, D_{eff} is the effective diffusion coefficient in the porous system and ε represents porosity.

Bruggeman's model,^[56,57] used in this work, relates the tortuosity factor to the volume fraction of the transporting phase:

$$\frac{D_{\text{eff}}}{D} = \varepsilon^{\gamma} \quad (10)$$

Therefore, the tortuosity value for the random porous media is $\tau = \varepsilon^{1-\gamma}$, where $\gamma = 1.5$ for porous system with spherical

particles and $\gamma = 2$ for cylindrical ones. In the ideal system (tortuosity do not affect the diffusion and conductivity), tortuosity is $\tau = 1$, giving the value of Bruggeman coefficient $\gamma = 1$.

In the real-life porous structures, the value of the tortuosity can vary from the theoretical values calculated using Bruggeman model. Djian et al.^[58] and Patel et al.^[59] measured the tortuosity of porous separator (Celgard 2400) obtaining Bruggeman coefficient $\gamma = 2.46$ and $\gamma = 2.8$, respectively. Doyle et al.^[21] reported the value $\gamma = 3.3$ for the LiMn₂O₄ electrode and $\gamma = 4.5$ for the p(VdF-HFP) polymer matrix.

In order to investigate the influence of the cathode tortuosity on the charge/discharge capacity of LIBs, the Bruggeman coefficient was changed between the values $\gamma = 1$ (ideal system), $\gamma = 1.5$ (spherical particles), $\gamma = 2$ (cylindrical particles) and $\gamma = 3$. With the porosity $\varepsilon_2 = 19.1\%$, this corresponds to the tortuosity values of $\tau = 1$, $\tau = 2.288$, $\tau = 5.236$ and $\tau = 27.412$, respectively. The resulting discharge and charge capacities are shown in Figure 11 and Figure S13, respectively.

For the cells with thin cathodes, the change of Bruggeman coefficient in the range $\gamma = 1$ to $\gamma = 1.5$ does not lead to changes in the charge and discharge capacity. Further increase of the Bruggeman coefficient leads to decrease in the specific capacity (especially for the fast charging). For the cells with ultra-thick cathodes the discharge and charge capacity de-

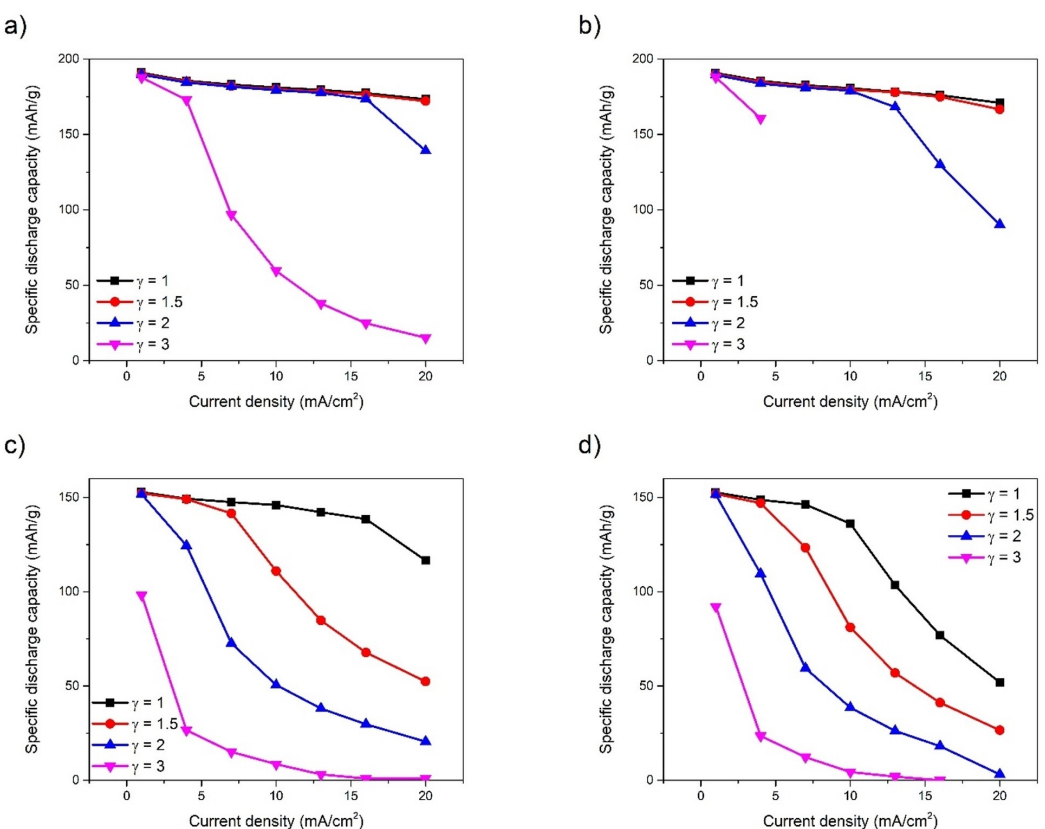


Figure 11. Specific discharge capacity of the battery cells a) cell 1, b) cell 2, c) cell 3, and d) cell 4; as a function of the applied current. Calculations performed for the Bruggeman coefficient (for the NMC electrode) changed in the range $\gamma=1$ to $\gamma=3$.

creases with the increase of Bruggeman coefficient in the entire investigated range.

It should be noted that the effect of the Bruggeman coefficient is stronger in the systems with lower porosity. In the systems with high porosity, like e.g., with the porosity $\varepsilon_2=41.7\%$, the change of Bruggeman coefficient from $\gamma=1$ to $\gamma=2$, corresponds to the tortuosity change between $\tau=1$ and $\tau=2.40$. In such systems the effect of the Bruggeman coefficient on the specific capacity is negligible even for the battery cells with ultra-thick cathode.

Separator width

Another parameter, which is very easy to modify in the experimental setup is the width of the separator. In this study the separator width was changed in the range 1 μm to 1 mm. The resulting discharge and charge capacities are shown in Figure 12 and Figure S14, respectively.

For cell 1, the width of the separator does not affect the response, as long as it is kept in the micrometre range. However, when it is increased to 1 mm, we observe the decrease in the charge and discharge capacity for the fast charging/discharging regime (i.e., current density higher than 10 mA/cm²).

The effect of the separator width changes on the charge capacity of cell 2 is identical as for cell 1. On the other hand, the discharge capacity of cell 2 is optimal for separator width $L_{\text{sep}}=100 \mu\text{m}$, and deviation from this value leads to the decrease in capacity, when the current density is higher than 10 mA/cm². This is due to the lithium depletion inside the NMC cathode.

The charge and discharge capacity of the cells with ultra-thick cathodes is optimal when the value of the separator width is kept low, i.e., below 10 μm for cell 3 and below 100 μm for cell 3. Increasing the separator width above this value leads to the decrease of the charge and discharge capacity in both fast and slow charging regime.

The width of the separators for most commercial lithium-ion batteries are in the range of 20–25 μm .^[60] Note, that while the model results show that L_{sep} should be kept under a certain threshold, in practical applications issues of energy and power density, mechanical strength and safety, need to be considered as well.

LIBs with thin separators often have lower internal resistance, and consequently exhibit high energy and power densities. However, thin separators may have adverse effects on the mechanical strength and safety. Thicker separators give greater mechanical strength and improved battery safety, but lead to lower energy and power densities. The performance of lithium-ion batteries is also greatly affected by the materials

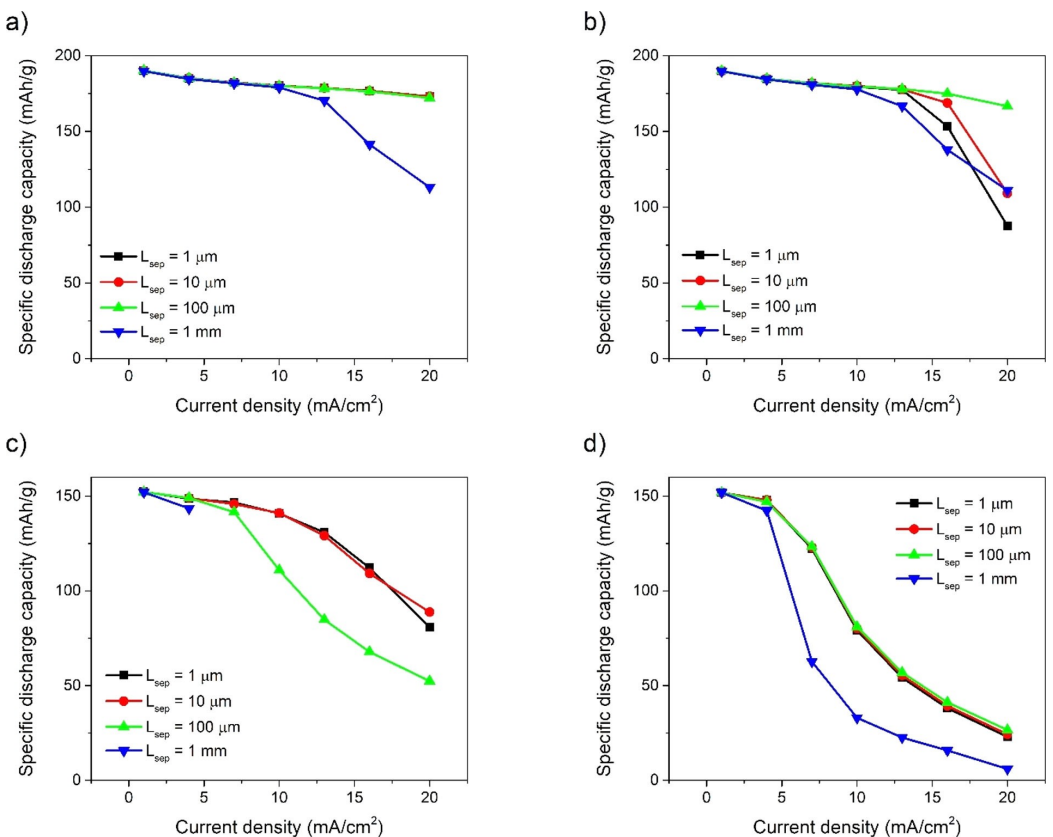


Figure 12. Specific discharge capacity of the battery cells a) cell 1, b) cell 2, c) cel 3, and d) cell 4; as a function of the applied current. Calculations performed for the separator width L_{sep} changed in the range 1 μm to 1 mm.

and structure of the separators. For more information about the requirements of separators for LIBs, see the extensive review.^[61]

Porosity distribution in the layered electrodes

In the section **Porosity**, we have observed, that the increase in porosity leads to the improvement of the overall capacity of the cells. The porosity was kept uniform in the cathode. In this section we will analyse the non-uniform porosity and the benefits of the porosity distribution in layered electrodes. Hence, we consider four types of cathodes, each consists of three layers of equal width but different porosities. The porosity heterogeneities of these cathodes are presented in the Figure 13. The discharge and charge capacity of four cells (as presented in Table 1) with layered cathodes are shown in Figure 14 and Figure S15, respectively.

Varying the porosity distribution has no effect on the cells with thin cathodes. However, when the ultra-thick cathodes are used, the specific capacity in fast charging/discharging regime (i.e., for current density higher than 5 mA/cm²) is higher for the electrodes with the porosity higher at the separator boundary.

The improved performance at high rates, for the cells with ultra-thick layers with high porosity close to separator (while maintaining same average porosity), is in the agreement with the calculations presented by Shodiev et al.^[62] as well as the



Figure 13. The porosity heterogeneities in the four types of cathodes. The electrodes are composed of three layers placed between the separator and the current collector (CC).

experimental results by Shodiev et al.,^[62] Wood et al.^[44] and Kalnas et al.^[63]

Summary and Conclusions

The computational models of electrochemical cells containing two types of anodes, namely the conversion Li-metal anode and intercalation graphite anode, as well as the NMC cathodes of varying thickness have been developed. These one-dimensional models were based on the classical Newman

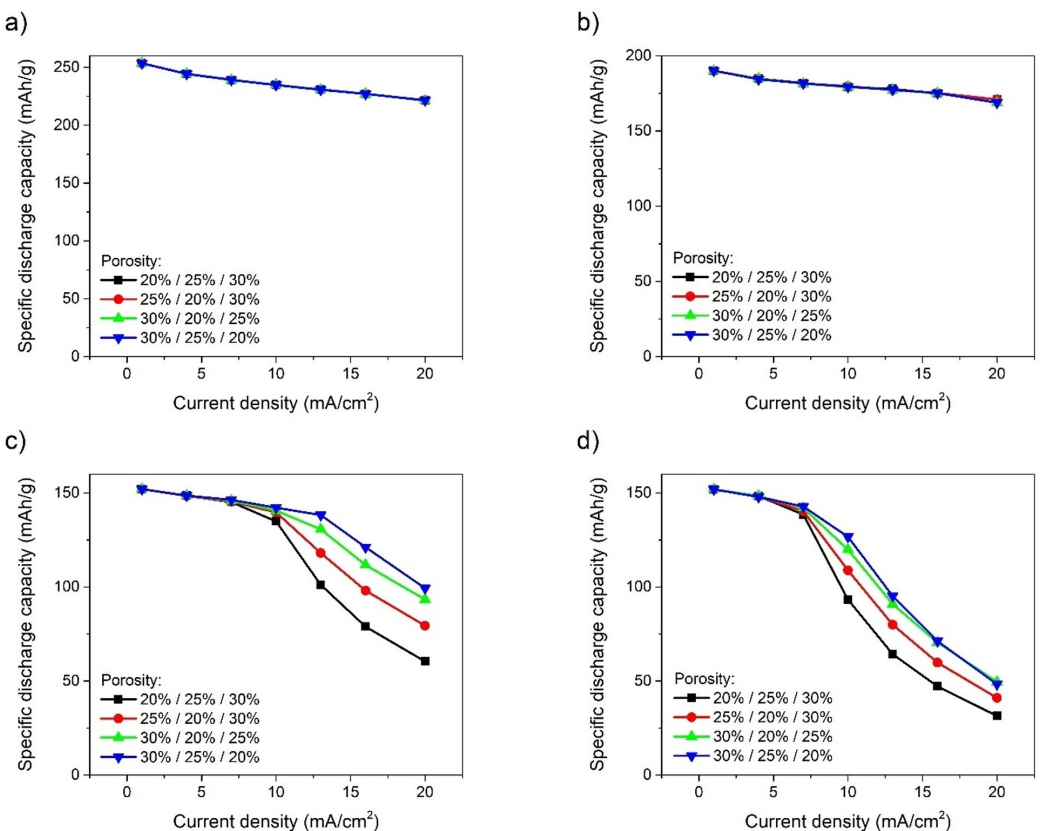


Figure 14. Specific discharge capacity of the battery cells a) cell 1, b) cell 2, c) cell 3, and d) cell 4; as a function of the applied current. Calculations were performed for the cathodes with varying porosity distribution.

equations^[20,21] and have been implemented in COMSOL Multiphysics. The electrolyte conductivity, the lithium diffusion coefficient, the transference number and the thermodynamic factor were described using the functions of concentration, obtained by Kremer et al.^[14] The step-by-step implementation instructions, which have been provided in the Supplementary Information, allows to easily recreate these models and after small modifications apply them to other Li-ion battery systems.

This work provides guidelines for conducting a numerical study of Li-ion battery systems, which includes performing the overpotential analysis to identify the potential losses and the sensitivity analysis to assess the influence of various parameters on the capacity of the cell.

Four investigated cells (i.e., cell 1 – conversion anode with thin NMC cathode, cell 2 – intercalation anode with thin NMC cathode, cell 3 – conversion anode with ultra-thick NMC cathode, and cell 4 – intercalation anode with ultra-thick NMC cathode) have been discharged and charged using applied currents in the range ± 1 to ± 20 mA/cm², which corresponds to a discharge/charge rate of 1 C to 20 C (for cells 1 and 2) and C/8 to 2.5 C (for cells 3 and 4). As expected, the discharge/charge capacity decreases with the increasing applied current, and this effect is significantly stronger for the cells containing ultra-thick cathodes.

The cells with the intercalation anodes show slightly smaller decrease of specific current capacity than the cells with the conversion anode.

The analysis of the factors contributing to the electrode overpotential clearly shows that the main contributor to the low capacity of the cells with ultra-thick cathodes at high currents is the electrolyte overpotential. The analysis of the lithium concentration profiles in the electrolyte shows the saturation and the depletion of lithium near the respective current collectors. This is in agreement with the results of Danner et al.,^[17] Zheng et al.,^[18] Gallagher et al.^[19] and Yu et al.,^[64] who demonstrated that transport within the electrolyte is the primary limitation factor for discharging ultra-thick electrodes, due to the existence of the concentration gradients forming between the electrodes and leading to non-uniform current distributions and underutilization of the active material.

The increase of the electrolyte salt concentration has no effect on the discharge capacity of the cells with thin NMC cathode, while the highest specific charge capacity is obtained when the electrolyte salt concentration is kept in the range from 1 M to 1.4 M. For the cells with ultra-thick cathode one can observe an improvement in capacity at high current densities, when the concentration is elevated.

While the discharge capacity of the cell containing lithium metal anode and ultra-thick cathode reaches the best response for the highest value of concentration (i.e., 2.3 M), the cell with

graphite anode and ultra-thick cathode reach the highest capacity for the salt concentration of 1.4 M. During charge, the highest capacity is obtained for the salt concentration of 1.4 M and begins to decrease with the further increase of salt concentration, for both cells with ultra-thick cathode. Knowing that the system with ultra-thick NMC cathode in the half-cell setup achieves the optimal discharge capacity for the electrolyte salt concentration equal 1.9 M,^[14] one can conclude that the optimal electrolyte concentration is not only a function of the cathode parameters but is influenced by the anode as well.

Several other parameters of the system have been investigated including NMC particle size, conductivity, reference exchange current density and the transfer coefficient. The electrolyte conductivity and the reference exchange current density (reaction rate) at the anode have negligible effect on the specific discharge and charge capacity. The reference exchange current density at the cathode has also no influence as long as it is kept higher than 1 A/m² (lower rate leads to worsening of the capacity). The very high value of the NMC particle radius (e.g., 100 µm) leads to low specific capacity. However, lowering the particle radius below the value of 10 µm leads to a very minor improvement of specific discharge/charge capacity. This is an extension to the observation of Du et al.,^[16] who suggested decreasing particle size as one of the possible engineering approaches (next to increasing molarity in the electrolyte) to overcome the limitations of cells with ultra-thick electrodes. In contrast to Du et al.,^[16] who investigated only two different values of particle radius, i.e., 2 µm and 0.5 µm (for LiNi_{0.8}Co_{0.15}Al_{0.05}O₂ cathode with the diffusion coefficient 1.5×10^{-15} m²/s), we have performed simulation for much wider range of particle sizes. That allowed us to identify the threshold value below which no further improvement in the cell response occurs (i.e., 10 µm for the NMC 622 cathode with the diffusion coefficient 2×10^{-13} m²/s).

The only parameter of the system that allows significant improvement of the specific capacity of the cells with ultra-thick electrode is the transference number. Increasing the transference number to 1, allow the cells with ultra-thick electrodes to operate at high charge/discharge currents with significantly lower capacity losses. When the transference number equals 1, the gradient of concentration does not occur in the system (the electrolyte salt concentration is constant in space and time). This can be achieved by using the membrane with negatively charged immobile sites in place of the classical state-of-art porous separator. However, applying this type of separator can lead to a drastic decrease of electrolyte conductivity, which consequently leads to a significant decrease in specific capacity of the cell.

Structure of the electrode is also important in the cell design. Namely the cathodes with high porosity and low tortuosity allow to achieve higher specific capacity. An interesting approach is to use the cathodes with varying porosity. Namely, the cells with the cathodes having higher porosity at separator boundary (while maintaining the average porosity constant), show increased value of the specific capacity. This agrees with experimental studies on layered electrodes.^[44,62,63]

In summary, the capacity losses in the cells with ultra-thick electrode come from the electrolyte overpotential, which is caused by the electrolyte salt concentration gradient. This gradient leads to the lithium depletion and saturation on the opposite sides of the cell, and consequently to underutilization of active materials and lithium plating, respectively. The electrolyte salt concentration gradient can be eliminated by applying the membrane with negatively charged immobile sites as the separator. Lithium depletion effect can be minimised, by elevating the initial electrolyte salt concentration. The optimal value of the salt concentration must be established on case-to-case basis, as it depends on the properties of both anode and cathode. Finally, the application of cells using conversion Li-metal anode allows to achieve slightly better cell capacity at high currents than when the intercalation graphite anode is used.

Supporting Information

In the Supporting Information, contains additional figures (Figures S1 to S15), as well as the step-by-step instructions for model implementation in COMSOL Multiphysics software. Additional files required for model implementation are also attached.

The authors have not cited any additional references within the Supporting Information.

Acknowledgements

This work was financed by ERC StG Bi3BoostFlowBat project (grant number 950038).

Conflict of Interests

The authors declare no conflict of interest.

Keywords: lithium-ion battery · lithium depletion · finite element modelling · overpotential analysis · influence of the parameters

- [1] J. M. Tarascon, M. Armand, *Nature* **2001**, *414*(6861), 359–67.
- [2] H. Takeshita, Portable Li-ion worldwide. *Proc. Conf. Power 2000*, San Diego, 25 September 2000.
- [3] R. Schmuck, R. Wagner, G. Hörpel, T. Placke, M. Winter, *Nat. Energy* **2018**, *3*(4), 267–78.
- [4] R. Moshtev, *J. Power Sources* **2000**, *91*, 86.
- [5] M. S. Whittingham, *Chem. Rev.* **2004**, *104*(10), 4271–301.
- [6] R. Marom, S. F. Amalraj, N. Leifer, D. Jacob, D. Aurbach, *J. Mater. Chem.* **2011**, *21*(27), 9938–54.
- [7] V. Etacheri, R. Marom, R. Elazari, G. Salitra, D. Aurbach, *Energy Environ. Sci.* **2011**, *4*(9), 3243–62.
- [8] J. B. Goodenough, K.-S. Park, *J. Am. Chem. Soc.* **2013**, *135*, 1167–1176.
- [9] N. Nitta, F. Wu, J. T. Lee, G. Yushin, *Mater. Today* **2015**, *18*(5), 252–64.
- [10] X. B. Cheng, R. Zhang, C. Z. Zhao, Q. Zhang, *Chem. Rev.* **2017**, *117*(15), 10403–73.
- [11] F. Wu, G. Yushin, *Energy Environ. Sci.* **2017**, *10*(2), 435–59.

- [12] X.-Q. Zhang, C.-Z. Zhao, J.-Q. Huang, Q. Zhang, *Engineering* **2018**, *4*, 831–847.
- [13] S. Megahed, B. Scrosati, *J. Pow. Sources* **1994**, *51*, 1–2.
- [14] L. S. Kremer, T. Danner, S. Hein, A. Hoffmann, B. Prifling, V. Schmidt, A. Latz, M. Wohlfahrt-Mehrens, *Batteries & Supercaps* **2020**, *3*, 1172–1182.
- [15] M. Singh, J. Kaiser, H. Hahn, *J. Electrochem. Soc.* **2015**, *162*(7), A1196–A1201.
- [16] Z. Du, D. L. Wood, C. Daniel, S. Kalnaus, J. Li, *J. Appl. Electrochem.* **2017**, *47*, 405–415.
- [17] T. Danner, M. Singh, S. Hein, J. Kaiser, H. Hahn, A. Latz, *J. Power Sources* **2016**, *334*, 191–201.
- [18] H. Zheng, J. Li, X. Song, G. Liu, V. S. Battaglia, *Electrochim. Acta* **2012**, *71*, 258–265.
- [19] K. G. Gallagher, S. E. Trask, C. Bauer, T. Woehrle, S. F. Lux, M. Tschech, P. Lamp, B. J. Polzin, S. Ha, B. Long, Q. Wu, W. Lu, D. W. Dees, A. N. Jansen, *J. Electrochem. Soc.* **2016**, *163*, A138–A149.
- [20] M. Doyle, T. F. Fuller, J. Newman, *J. Electrochem. Soc.* **1993**, *140*, 1526.
- [21] M. Doyle, J. Newman, A. S. Gozdz, C. N. Schmutz, J. M. Tarascon, *J. Electrochem. Soc.* **1996**, *143*, 1890.
- [22] <https://www.comsol.com/>.
- [23] K. E. Thomas, J. Newman, R. M. Darling, in *Advances in Lithium-Ion Batteries* (Eds. W. A. van Schalkwijk, B. Scrosati), Kluwer Academic/Plenum Publishers, NY **2002**, pp. 345–392.
- [24] G. G. Botte, V. R. Subramanian, R. E. White, *Electrochim. Acta* **2000**, *45*(15–16), 2595–2609.
- [25] P. M. Gomadam, J. W. Weidner, R. A. Dougal, R. E. White, *J. Power Sources* **2002**, *110*(2), 267–284.
- [26] S. Santhanagopalan, Q. Guo, P. Ramadass, R. E. White, *J. Power Sources* **2006**, *156*(2), 620–628.
- [27] G. G. Botte, B. A. Johnson, R. E. White, *J. Electrochem. Soc.* **1999**, *146*, 914–923.
- [28] L. Cai, R. E. White, *J. Power Sources* **2011**, *196*(14), 5985–5989.
- [29] M. Guo, G.-H. Kim, E. White, *J. Power Sources* **2013**, *240*, 80–94.
- [30] G. Sikha, B. N. Popov, R. E. White, *J. Electrochem. Soc.* **2004**, *151*, A1104.
- [31] D. J. Pereira, A. M. Aleman, J. W. Weidner, T. R. Garrick, *J. Electrochem. Soc.* **2022**, *169*, 020577.
- [32] R. Darling, J. Newman, *J. Electrochem. Soc.* **1997**, *144*(12), 4201–4208.
- [33] S. Santhanagopalan, R. E. White, *Int. J. Electrochem.* **2012**, *2012*, 395838.
- [34] J. P. Meyers, M. Doyle, R. M. Darling, J. Newman, *J. Electrochem. Soc.* **2000**, *147*(8), 2930–2940.
- [35] Z. Chen, D. L. Danilov, L. H. J. Raijmakers, K. Chayambuka, M. Jiang, L. Zhou, J. Zhou, R.-A. Eichel, P. H. L. Notten, *J. Power Sources* **2021**, *509*, 230345.
- [36] Z. Cao, M. Hashinokuchi, T. Doi, M. Inaba, *J. Electrochem. Soc.* **2019**, *166*, A82–A88.
- [37] V. Srinivasan, J. Newman, *J. Electrochem. Soc.* **2004**, *151*, A1517–A1529.
- [38] Y. Yamada, A. Yamada, *J. Electrochem. Soc.* **2015**, *162*, A2406–A2423.
- [39] Y. Yamada, J. Wang, S. Ko, E. Watanabe, A. Yamada, *Nat. Energy* **2019**, *4*, 269–280.
- [40] Y. Yamada, *BCSJ* **2019**, *93*, 109–118.
- [41] A. Latz, J. Zausch, *Electrochem. Adv. Mater. Technol. Instrum.* **2013**, *110*, 358–362.
- [42] H. Yang, N. Wu, *Energy Sci. Eng.* **2022**, *10*, 1643–1671.
- [43] S. C. Kim, J. Wang, R. Xu, P. Zhang, Y. Chen, Z. Huang, Y. Yang, Z. Yu, S. T. Oyakhire, W. Zhang, L. C. Greenburg, M. S. Kim, D. T. Boyle, P. Sayavong, Y. Ye, J. Qin, Z. Bao, Y. Cui, *Nat. Energy* **2023**. <https://doi.org/10.1038/s41560-023-01280-1>.
- [44] M. Wood, J. Li, Z. Du, C. Daniel, A. R. Dunlop, B. J. Polzin, A. N. Jansen, G. K. Krumdick, D. L. Wood, *J. Power Sources* **2021**, *515*, 230429.
- [45] T. Shi, Q. Tu, Y. Tian, Y. Xiao, L. J. Miara, O. Kononova, G. Ceder, *Adv. Energy Mater.* **2020**, *10*, 1902881.
- [46] SHIMADZU, Application News No. PSA-2201 Powder Property Analysis Particle Size Distribution Measurement of Lithium-Ion Battery Materials, https://www.ssi.shimadzu.com/sites/ssi.shimadzu.com/files/pim/pim_document_file/ssi/applications/application_note/16960/PSA-2201-particle-size-of-battery-materials.pdf.
- [47] A. C. Wagner, N. Bohn, H. Geßwein, M. Neumann, M. Osenberg, A. Hilger, I. Manke, V. Schmidt, J. R. Binder, *ACS Appl. Energ. Mater.* **2020**, *(12)*, 12565–12574.
- [48] R. Amin, Y.-M. Chiang, *J. Electrochem. Soc.* **2016**, *163*, A1512–A1517.
- [49] Q. Lin, J. N. Harb, *J. Electrochem. Soc.* **2004**, *151*, A1115.
- [50] R. Tang, Q. Yun, W. Lv, Y. B. He, C. You, F. Su, L. Ke, B. Li, F. Kang, Q. H. Yang, *Carbon* **2016**, *103*, 356–362.
- [51] W. Guoping, Z. Qingtang, Y. Zuolong, Q. MeiZheng, *Solid State Ionics* **2008**, *179*, 263–268.
- [52] Z. Du, J. Li, M. Wood, C. Mao, C. Daniel, D. L. Wood III, *Electrochim. Acta* **2018**, *270*, 54–61.
- [53] Y. Liu, X. Li, H. Guo, Z. Wang, W. Peng, Y. Yang, R. Liang, *J. Power Sources* **2008**, *184*, 522–526.
- [54] S. Jessl, D. Beesley, S. Engelke, C. J. Valentine, J. C. Stallard, N. Fleck, S. Ahmad, M. T. Cole, M. De Volder, *Mat. Sci. Eng. A* **2018**, *735*, 269–274.
- [55] A. Varzi, C. Täubert, M. Wohlfahrt-Mehrens, *Electrochim. Acta* **2012**, *78*, 17–26.
- [56] D. A. G. Bruggeman, *Annalen der Physik* **1935**, *416*(7), 636–664.
- [57] B. Tjaden, S. J. Cooper, D. J. L. Brett, D. Kramer, P. R. Shearing, *Curr. Opinion Chem. Engineering* **2016**, *12*, 44–51.
- [58] D. Djian, F. Alloin, S. Martinet, H. Lingnier, J. Y. Sanchez, *J. Power Sources* **2007**, *172*, 416–421.
- [59] K. K. Patel, J. M. Paulsen, J. Desilvestro, *J. Power Sources* **2003**, *122*, 144–152.
- [60] M. R. Palacín, *Chem. Soc. Rev.* **2009**, *38*, 2565–2575.
- [61] H. Lee, M. Yanilmaz, O. Toprakci, K. Fu, X. Zhang, *Energy Environ. Sci.* **2014**, *7*(12), 3857–3886.
- [62] A. Shodiev, M. Chouchane, M. Gaberscek, O. Arcelus, J. Xu, H. Oularbi, J. Yu, J. Li, M. Morcrette, A. A. Franco, *Energy Storage Mater.* **2022**, *47*, 462–471.
- [63] S. Kalnaus, K. Livingston, W. B. Hawley, H. Wang, J. Li, *J. Energy Storage* **2021**, *44*, 103582.
- [64] D. Y. W. Yu, K. Donoue, T. Inoue, M. Fujimoto, S. Fujitani, *J. Electrochem. Soc.* **2006**, *153*, A835–A839.

Manuscript received: May 8, 2023

Revised manuscript received: July 20, 2023

Accepted manuscript online: August 4, 2023

Version of record online: August 17, 2023